Available online at www.sciencedirect.com
ScienceDirect
Journal of Computational Physics 223 (2007) 589–608
JOURNAL OF COMPUTATIONAL PHYSICS
www.elsevier.com/locate/jcp

Unified solver for rarefied and continuum flows with adaptive mesh and algorithm refinement

V.I. Kolobov [a,*], R.R. Arslanbekov [a], V.V. Aristov [b], A.A. Frolova [b], S.A. Zabelok [b]

[a] CFD Research Corporation, 215 Wynn Dr, Huntsville, AL 35805, USA
[b] Dorodnicyn Computing Center of the Russian Academy of Science, Moscow, Russia

Received 8 December 2005; received in revised form 25 September 2006; accepted 26 September 2006
Available online 13 November 2006

Abstract

This paper describes a Unified Flow Solver (UFS) for rarefied and continuum gas flows. The UFS separates the rarefied and continuum flow domains and selects appropriate solvers to combine the efficiency of continuum models with the accuracy of kinetic models. The direct numerical solution of the Boltzmann transport equation is used in rarefied regions, while kinetic schemes of continuum fluid dynamics are used elsewhere. Using similar computational techniques for the kinetic and continuum solvers, and employing intelligent domain decomposition algorithms attain the efficiency and numerical stability of the UFS. Solutions of test problems are presented to illustrate the capabilities of the UFS for high and low speed flows. It is shown that the UFS can dynamically adapt the computational mesh and automatically introduce and remove kinetic patches to provide significant savings by limiting molecular scale solutions only to the regions where they are needed.

Keywords: Rarefied gas dynamics; Boltzmann kinetic equation; Hybrid methods; Adaptive mesh and algorithm refinement; Unified flow solver

1. Introduction

The presence of rarefied and continuum domains is a typical feature of many complex gas flows. In rarefied domains, the mean free path of gas molecules is comparable or larger than a characteristic scale of the system. These domains are naturally described by particle models such as the Direct Simulation Monte Carlo (DSMC) or involve solutions of the Boltzmann kinetic equation for the velocity distribution function. The continuum domains are best described by the fluid (Euler or Navier Stokes) equations in terms of average flow velocity, gas density and temperature. The development of hybrid solvers combining kinetic and fluid models has been an important area of research over the last decade (see Refs. [1,2] for reviews). Potential applications of such

* Corresponding author. Tel.: +1 256 726 4847.
E-mail address: vik@cfdrc.com (V.I. Kolobov).

0021-9991/$ - see front matter © 2006 Published by Elsevier Inc.
doi:10.1016/j.jcp.2006.09.021

solvers range from high altitude flights to gas flows in micro systems. The key parameter defining the choice of the appropriate physical model is the local Knudsen number, *Kn*, defined as the ratio of the mean free path to the characteristic size of the system. For high altitude flights, it is the low gas density, for gas flows in micro systems, it is a small dimension of the system that dictates the choice of a kinetic model.

Key challenges in the development of hybrid codes are the identification of kinetic /continuum domains, the choice of a coupling method and imposition of boundary conditions at interfaces. Different methods explored to date can be classified into three categories. The first category includes methods employing domain decomposition in physical space. In this category, the computational domain is decomposed into kinetic and continuum sub-domains using appropriate criteria [3–12]. The second category includes methods based on domain decomposition in velocity space where fast and slow particles are treated separately [13]. The third category includes hybrid models. With these methods, one solves both kinetic and fluid equations in the entire domain and uses the Velocity Distribution Function (VDF) to compute transport coefficients for the fluid equations [14,15].

Most of the published works fall into the first category. Typically, particle methods such as DSMC or Molecular Dynamics are used in regions with strong deviations from equilibrium, and a fluid (Euler or NS) solver is used in other regions. An adaptive mesh and algorithm refinement (AMAR) procedure has been developed for a DSMC-based particle method to supplement the grid refinement by algorithm refinement (continuum vs atomistic) based on continuum breakdown criteria [16]. However, statistical noise inherent to DSMC has been identified as an obstacle for the development of hybrid solvers [17,18]. Due to strong fluctuations of the macroparameters calculated from the DSMC, the problem of connecting kinetic and continuum regions is complicated by severe stability problems when DSMC data is handed over to a continuum solver at the interface. The uniqueness of our approach consists of combining direct numerical solution (DNS) of the BTE with kinetic schemes of gas dynamics in a hybrid code with solution adaptive domain decomposition [19]. The DNS has recently emerged as a viable alternative to DSMC [20,21] and is preferable to DSMC for coupling kinetic and continuum models because similar numerical techniques are used for solving both the Boltzmann and continuum equations. The recent efforts to combine DNS with a NS solver [22] used a priory decomposition of the domain, rather than solution adaptive dynamic domain decomposition employed in our work.

The key components of the UFS are shown in Fig. 1. The main component is a Boltzmann solver implemented with the DNS method for the UFS described in this paper. Another component is a Computational Fluid Dynamics (CFD) solver. It is preferable to implement such a solver using numerical algorithms similar to the Boltzmann solver. From this point of view, recently introduced kinetic schemes of gas dynamics are very

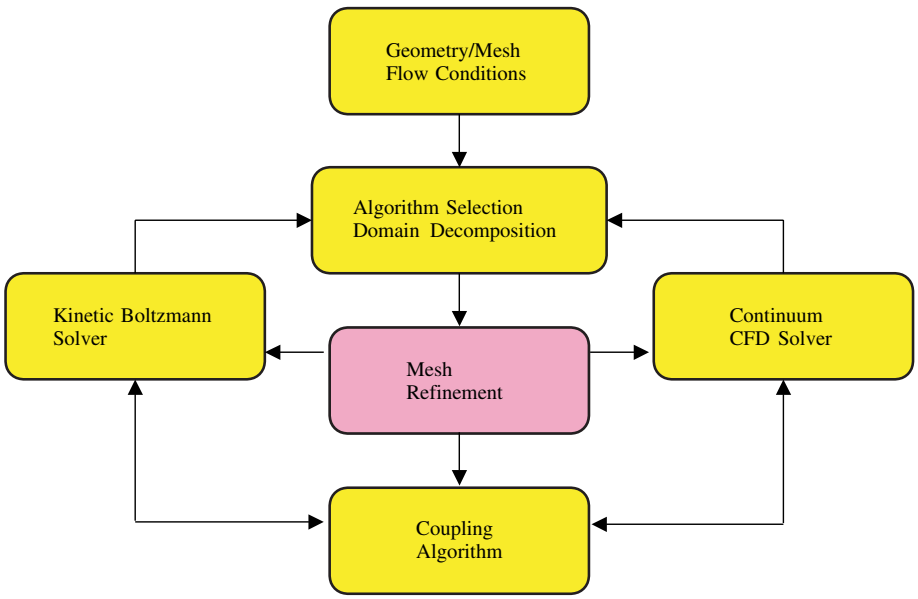

Fig. 1. Key UFS components.

attractive [23,24]. The remaining components of the UFS contain criteria for domain decomposition into kinetic and continuum parts and coupling algorithms.

The open source Gerris Flow Solver (GFS) [25] is used as a framework for the UFS. The original Gerris code contained an incompressible flow solver with a binary tree-based dynamically adaptive grid and support of complex boundaries. The code can automatically generate Cartesian mesh around embedded objects defined through standard files. Using the GFS framework, we have added a Boltzmann solver for one component monatomic gases, compressible Euler and NS solvers based on kinetic scheme, and developed practical criteria for domain decomposition and coupling kinetic and CFD solvers. The UFS can perform dynamic adaptation of the mesh for the solution and geometry, identify kinetic and continuum domains and select appropriate solvers based on continuum breakdown criteria.

The structure of the paper is as follows. Section 2 describes DNS methods for the Boltzmann equation and presents examples of rarefied flow simulations using the Boltzmann solver. Section 3 describes kinetic schemes for the Euler and NS equations. Section 4 is devoted to continuum breakdown criteria, domain decomposition into kinetic and continuum patches and coupling kinetic and continuum solvers. Section 5 illustrates current capabilities of the UFS.

2. Numerical solution of the Boltzmann equation

The Boltzmann Transport Equation (BTE) describes the evolution of a particle distribution function, f, in a six-dimensional phase space [26]

$$\frac{\partial f}{\partial t} + \nabla_r \cdot (\boldsymbol{\xi} f) = I(f,f). \tag{1}$$

Here $\mathbf{r}$ is a position vector in physical space, $\boldsymbol{\xi}$ is the velocity vector and t is time. The right-hand side of Eq. (1) contains an integral operator describing binary collisions among particles. For elastic collisions in a monatomic gas, it has the following form:

$$I(\boldsymbol{\xi}) = \int_{S^2} \mathrm{d}\boldsymbol{\omega} \int_{R^3} (f(\boldsymbol{\xi}_1')f(\boldsymbol{\xi}') - f(\boldsymbol{\xi}_1)f(\boldsymbol{\xi}))g\sigma(g,\chi)\,\mathrm{d}\boldsymbol{\xi}_1 = -\nu(\boldsymbol{\xi})f + \Phi. \tag{2}$$

Here ν is the collision frequency, Φ is the inverse collision integral, $g = |\boldsymbol{\xi}_1 - \boldsymbol{\xi}|$ is the relative velocity of the colliding particles, $\boldsymbol{\omega}$ is a vector on a unit sphere S^2 in velocity space and $\mathrm{d}\boldsymbol{\omega}$ is an element of the area of the surface of this sphere, $\sigma(g,\chi)$ is the differential collision cross section, χ is the scattering angle and $\mathrm{d}\boldsymbol{\xi} = \mathrm{d}\xi_x\mathrm{d}\xi_y\mathrm{d}\xi_z$. The post-collision velocities $(\boldsymbol{\xi}', \boldsymbol{\xi}_1')$ and the pre-collision velocities $(\boldsymbol{\xi}, \boldsymbol{\xi}_1)$ satisfy the momentum and energy conservation laws

$$\begin{aligned} &\boldsymbol{\xi} + \boldsymbol{\xi}_1 = \boldsymbol{\xi}' + \boldsymbol{\xi}_1', \\ &|\boldsymbol{\xi}|^2 + |\boldsymbol{\xi}_1|^2 = |\boldsymbol{\xi}'|^2 + |\boldsymbol{\xi}_1'|^2. \end{aligned} \tag{3}$$

The integral (2) can also be written in the form

$$I(\boldsymbol{\xi}) = \int_0^{2\pi} \mathrm{d}\varepsilon \int_0^{b_m} \mathrm{d}b \int_{R^3} (f(\boldsymbol{\xi}_1')f(\boldsymbol{\xi}') - f(\boldsymbol{\xi}_1)f(\boldsymbol{\xi}))gb\,\mathrm{d}\boldsymbol{\xi}_1, \tag{4}$$

where b is the impact parameter (defined as the distance of the closest approach of the trajectories) usually bounded by a certain value b_m, and ε is the azimuth impact angle. The scattering angle $\chi(g,b)$ depends on the scattering potential of inter-atomic interactions. For the Hard Sphere (HS) molecules of diameter d, the scattering is isotropic and $b = d\sin\theta$ where $\theta = (\pi - \chi)/2$. For the Variable Hard Sphere (VHS) models frequently used in DSMC simulations, the scattering is also isotropic and $g\sigma = C_k g^{1-4/k}$, where k is the exponent in the intermolecular potential. For other commonly used scattering potentials, these relationships can be found in [27]. We have implemented the following scattering models: the HS model, the inverse power repulsive potentials, the Lennard-Jones potential and the Coulomb potential.

For the numerical solution of Eq. (1), a Cartesian mesh in velocity space is introduced with a cell size $\Delta\boldsymbol{\xi}$ and nodes $\boldsymbol{\xi}_i$. Using this mesh, Eq. (1) is reduced to a system of linear hyperbolic transport equations in physical space with a nonlinear source term

$$\frac{\partial f_i}{\partial t} + \nabla_{\mathbf{r}} \cdot (\boldsymbol{\xi}_i f_i) = I(f_i, f_i). \tag{5}$$

Introducing a computational grid in physical space, we split the solution of (5) into two stages: collisionless flow and relaxation. For the collisionless flow, we use an explicit finite volume numerical scheme (index j denotes cell number in physical space)

$$V\frac{f_{ij}^{*k} - f_{ij}^{k-1}}{\Delta t} + \sum_{\text{face}} (\boldsymbol{\xi}_i \cdot \mathbf{n})_{\text{face}} f_{i,\text{face}}^{k-1} S_{\text{face}} = 0. \tag{6}$$

Here k is the time index, $*$ denotes the intermediate time level, $f_{i,\text{face}}^{k-1}$ is the value of the function on the cell face, $\mathbf{n}$ is the unit outward normal vector to the face, V is the cell volume and S_{face} is the face surface area. For calculation of the face values of the distribution function, we use standard interpolation schemes of the first and second order. The second-order scheme has three options: (i) no limiter, (ii) the minmod limiter and (iii) van Leer limiter. A binary tree-based dynamically adaptive isotropic Cartesian grid with a local mesh size h is automatically generated in a computational domain using the GFS engine [25].

The relaxation stage has the form

$$\frac{f_{ij}^{k} - f_{ij}^{*k}}{\Delta t} = -\nu_{ij}^{*k} f_{ij}^{*k} + \Phi_{ij}^{*k}. \tag{7}$$

Currently, we use an explicit scheme with automatic selection of the time step. The time step is selected as $\Delta t = \min(\Delta t_{\text{adv}}, \Delta t_{\text{col}})$ where $\Delta t_{\text{adv}} = h/|\boldsymbol{\xi}_{\max}|$ and $\Delta t_{\text{col}} = 1/\nu_{\max}$. Here $|\boldsymbol{\xi}_{\max}|$ is the absolute value of the maximum particle velocity, $\nu_{\max}$ is the maximum value of the collision frequency. For instance, in a Knudsen layer (the area of large spatial gradients and highly non-equilibrium velocity distribution function), the spatial size of the local cell should be smaller than the local mean free path. Additional decrease of the time step is dictated by the value of $\nu_{\max}$. Since the collision integral is calculated using a quasi-statistical procedure (see below), some oscillations of the collision frequency $\nu(\boldsymbol{\xi})$ can appear on periphery of the velocity space. This results in an additional increase of the collision frequency $\nu_{\max}$ and a considerable decrease of the time step. This additional limitation on the time step for Eq. (7) allows one to use the splitting method even for small Kn numbers. For transient problems, the time step must be selected using the minimal time step for the entire computational domain. It should be noted that with conservatively calculated collision integrals, it is possible to use computational schemes without splitting into collisionless flow and relaxation.

The boundary conditions at the surface of solid objects define the distribution function of the reflected particles as a sum of diffuse and specular reflections with an accommodation coefficient α

$$f(\boldsymbol{\xi}) = \alpha f_{\text{M}}(\boldsymbol{\xi}) + (1-\alpha) f_r(\boldsymbol{\xi}). \tag{8}$$

The specular reflection term is $f_r = f(\xi_r)$, where ξ_r is the velocity of an incoming molecule towards the boundary, which after specular reflection transforms into $\boldsymbol{\xi}_r = \boldsymbol{\xi} - 2(\boldsymbol{\xi} \cdot \mathbf{n})\mathbf{n}$ where $\mathbf{n}$ is a unit vector normal to the boundary. The diffuse reflection term contains the Maxwellian distribution $f_{\text{M}}(\boldsymbol{\xi})$ with a zero mean velocity, depending on the temperature of the boundary, T_{w} and the gas density n_{w} calculated to ensure zero particle flux at the boundary at a given point. At the boundaries of computational domain, for many problems, the distribution function can be assumed as Maxwellian $f_{\text{M}}(\boldsymbol{\xi})$ with a mean velocity $\mathbf{U}$ for $(\boldsymbol{\xi} \cdot \mathbf{n}) > 0$. For parts of the boundary with $(\boldsymbol{\xi} \cdot \mathbf{n}) < 0$, the distribution function is found from the solution.

The computational domain in velocity space is selected in such a way that the values of the distribution function outside of the domain are negligible. For two-dimensional problems (in physical space), one half of the velocity space ($\xi_z > 0$) can be used.

2.1. Calculation of the collision integral

The main problem in solving the Boltzmann equation consists in evaluating the collision integral [28]. The calculation of the five-fold integrals (2) or (4) represents a challenge with respect to efficiency and precision. We used the discrete analog of the collision integral having the following properties:

(i) The integral is equal to zero for a Maxwellian distribution, $I(f_M,f_M) = 0$.
(ii) The distribution remains positive for all nodes in velocity space, when the relaxation problem (7) is solved.
(iii) For the collision invariants, $\psi(\boldsymbol{\xi}) = (1, \boldsymbol{\xi}, \xi^2)$, the conservation laws should be satisfied

$$\int_{\mathbb{R}^3} \psi I(f,f)\,\mathrm{d}\boldsymbol{\xi} = 0. \tag{9}$$

Below, we briefly review different methods of calculating the collision integral and describe the methods used in the present paper. For brevity, we omit the second (spatial) index of f in this section.

2.1.1. The NtN method

The first type of methods can be called Node to Node (NtN). This method has been used by Goldstein et al. [29], Buet [30], Rogier and Schneider [31], Tan and Varghese [32] and Frolova and co-workers [2]. To illustrate the essence of the method, Fig. 2 shows a collision sphere in velocity space. This sphere with center $\boldsymbol{\xi}_0 = (\boldsymbol{\xi}_i + \boldsymbol{\xi}_j)/2$ and radius $|g|/2$ is wrapped around pre- and post collision velocities (see Eqs. (3)). The NtN method takes into account only those post-collisional velocities that fall exactly into the nodes of the velocity grid. Therefore all properties (i–iii) are satisfied automatically.

For the numerical calculation by the NtN method, the integral (2) can be written in a symmetric form [32]

$$I(\boldsymbol{\zeta}) = \frac{1}{2}\int_{S^2} \mathrm{d}\boldsymbol{\omega} \int_{R^3}\int_{R^3} (\delta(\boldsymbol{\xi}'_1 - \boldsymbol{\zeta}) + \delta(\boldsymbol{\xi}' - \boldsymbol{\zeta}) - \delta(\boldsymbol{\xi}_1 - \boldsymbol{\zeta}) - \delta(\boldsymbol{\xi} - \boldsymbol{\zeta}))f(\boldsymbol{\xi})f(\boldsymbol{\xi}_1)g\sigma(g,\boldsymbol{\omega})\,\mathrm{d}\boldsymbol{\xi}\,\mathrm{d}\boldsymbol{\xi}_1, \tag{10}$$

where $\delta(\boldsymbol{\xi})$ denotes the delta-function. This representation is better for the numerical evaluation because direct and inverse collisions are treated symmetrically and microscopic reversibility is satisfied. For the numerical evaluation, the 8-fold integral (10) is written in the form [32]

$$I(\boldsymbol{\zeta}) = \frac{(\Delta\xi)^6}{2}\sum_i^N \sum_j^N f_i f_j \int_{S^2} \mathrm{d}\boldsymbol{\omega}[\Delta_i + \Delta_j] g_{ij}\sigma_{ij}(\boldsymbol{\omega}), \tag{11}$$

where $\Delta_i = \delta(\boldsymbol{\xi}'_i - \boldsymbol{\zeta}) - \delta(\boldsymbol{\xi}_i - \boldsymbol{\zeta})$, $\Delta_j = \delta(\boldsymbol{\xi}'_j - \boldsymbol{\zeta}) - \delta(\boldsymbol{\xi}_j - \boldsymbol{\zeta})$ and N is the total number of nodes in velocity space.

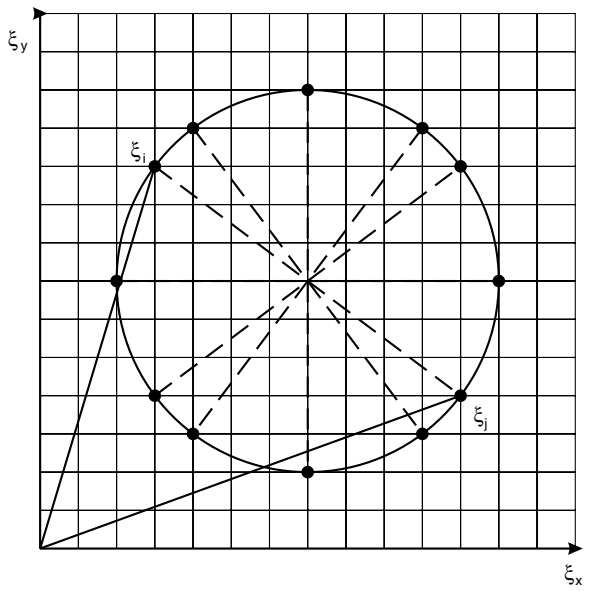

Fig. 2. Collision sphere in the (ξ_x, ξ_y) plane. ξ_i and ξ_j are pre-collision velocity nodes. Points denote post-collision velocity nodes taken into account in the NtN method.

To evaluate the integral over the unit sphere in (11) ensuring the exact energy conservation, the NtN method takes into account only those post-collisional velocity nodes that lie on the collisional sphere (see Fig. 2)

$$\int_{S^2} \mathrm{d}\boldsymbol{\omega}[\Delta_i + \Delta_j]\sigma_{ij}(\boldsymbol{\omega}) = \sum_{l}^{M_{ij}} w_{ijl}[\Delta_i + \Delta_j], \tag{12}$$

where M_{ij} is the total number of such nodes (for each pair of pre-collisional nodes i and j) and w_{ijl} are their weights. For the VHS-like models with isotropic scattering, the number and position of nodes on the collisional sphere can be determined a priory and the calculation of weights is simple, $w_{ijl} \sim 1/M_{ij}$. For more general potentials, the angle between direct and inverse collisions is a function of relative velocity and these calculations become cumbersome.

The NtN method is conservative and requires no interpolation of the velocity distribution function. For good accuracy, a rather dense mesh in velocity space has to be used. If all velocity nodes are used, the method is deterministic. The evaluation of integral in this case requires $O(N^2)$ operations. To reduce the number of operations it is possible to select collision events using Monte Carlo method [32], or use Korobov sequences (see below). The disadvantages of the method are (i) only a small number of post-collision velocities distributed over collisional spheres fall exactly into the velocity grid and (ii) the method is applicable only for VHS-like models with isotropic scattering. The NtN method cannot be extended for general models of intermolecular interactions and for non-uniform grid in velocity space because only selected post-collisional velocities are used. Also, extensions to gas mixtures with arbitrary molecular mass ratios are difficult.

2.1.2. Tcheremissine's method

To generalize the NtN method for more complex models of molecular collisions it is necessary to take into account inverse collisions that do not fall exactly into the nodes of the velocity grid. Depending on how the post collision velocities are taken into account it is possible to obtain different schemes for calculation of the integral. In a series of works (see [21,27,33] and references therein) Tcheremissine developed conservative methods of calculating collision integral for arbitrary interaction potentials, by dividing contributions of post collision points into two parts and accounting them in the two closest nodes (see Fig. 3). This method allows one to satisfy conservation laws (3) in each collision. The method is briefly described below.

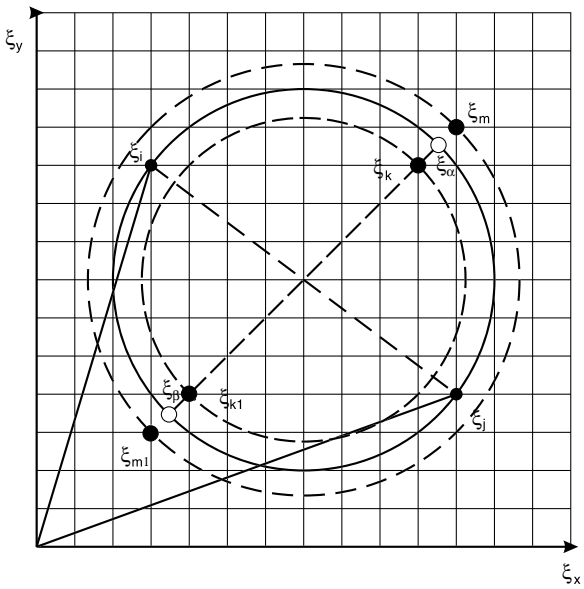

Fig. 3. Selection of post-collision nodes for Tcheremissine's method.

For arbitrary potential on intermolecular interactions, it is more convenient to perform integration over collision impact parameters (4) instead of integration over a unit sphere (2). The corresponding integral in the symmetric form with respect to direct and inverse collisions is

$$I(\zeta) = \frac{1}{4}\int_0^{2\pi} \mathrm{d}\varepsilon \int_0^{b_m} \mathrm{d}b \int_{R^3}\int_{R^3} [\delta(\xi-\zeta)+\delta(\xi_1-\zeta)-\delta(\xi'-\zeta)-\delta(\xi_1'-\zeta)]\Omega(\xi,\xi_1)bg\,\mathrm{d}\xi_1\,\mathrm{d}\xi, \tag{13}$$

where $\Omega(\xi,\xi_1) = f(\xi')f(\xi_1') - f(\xi)f(\xi_1)$. On the discrete velocity grid, the velocities before collision (ξ_i,ξ_j) are selected at integer nodes i, j of the grid and the post collision velocities (ξ_α,ξ_β) do not necessarily fall into the nodes. To obtain the mass, impulse and energy conservation in each collision and satisfy the condition $\psi(\xi_i)+\psi(\xi_j) = \psi(\xi_\alpha)+\psi(\xi_\beta)$, the value of $\psi(\xi_\alpha)+\psi(\xi_\beta)$ is interpolated to the nearest integer nodes ξ_k, ξ_m using the following interpolation:

$$\psi(\xi_\alpha)+\psi(\xi_\beta) = (1-r)(\psi(\xi_m)+\psi(\xi_{m1})) + r(\psi(\xi_k)+\psi(\xi_{k1})), \tag{14}$$

where the nodes ξ_{k1}, ξ_{m1} are selected symmetrically with respect to the nodes ξ_k, ξ_m (see Fig. 3). On a uniform grid, it is possible to perform this interpolation with one coefficient for five scalar invariant functions of vector ψ, since conservation of mass and impulse in this case is satisfied automatically due to the symmetric position of the nodes. The coefficient r is found from the equation

$$\xi_\alpha^2+\xi_\beta^2 = (1-r)(\xi_m^2+\xi_{m1}^2) + r(\xi_k^2+\xi_{k1}^2). \tag{15}$$

The weight coefficients r and $1-r$ define the parts of the contribution $\Omega(\xi_\alpha,\xi_\beta) = f(\xi_i)f(\xi_j) - f(\xi_\alpha)f(\xi_\beta)$ to the closest integer nodes ξ_k, ξ_{k1}, ξ_m, ξ_{m1}, $\Omega(\xi_m,\xi_{m1}) = (1-r)\Omega(\xi_\alpha,\xi_\beta)$, $\Omega(\xi_k,\xi_{k1}) = r\Omega(\xi_\alpha,\xi_\beta)$ (see Fig. 3). The calculation of the scattering angle $\theta(g,b)$ as function of collision parameters for complicated molecular potentials is described in [27,33]. An interpolation of the VDF for calculation of $f(\xi')f(\xi_1')$ is required but it can be performed using any interpolation formula and does not influence the conservation laws.

2.1.3. The NtCN method

Finally, we describe a method that can be used for arbitrary interaction potentials and non-uniform grid in velocity space. We start from the same symmetric form of the collision integral as in Tcheremissine's method.

The procedure of calculating collision integral consists of the following steps (see Fig. 4):

(i) select pre-collision velocities ξ_i, ξ_j for impact parameters b, ε,
(ii) determine post-collision velocities ξ_μ, ξ_λ,
(iii) find nodes ξ_m, ξ_k closest to the nodes ξ_μ, ξ_λ,
(iv) calculate an inverse collision with velocities ξ_m, ξ_k for the same impact parameters b, ε,
(v) calculate velocities after this inverse collision ξ_α, ξ_β,
(vi) calculate contributions to the integral from direct $\Omega(\xi_i,\xi_j)g_{ij}b$ and inverse $\Omega(\xi_m,\xi_k)g_{mk}b$ collisions, where the quantities $f_\alpha f_\beta, f_\lambda f_\mu$ are found using a logarithmic interpolation to give zero integral for Maxwellian distribution,
(vii) sum up contributions to the collision integral $-\nu(\xi_i)f(\xi_i)+\Phi(\xi_i)$.

This procedure of evaluating collision integral uses closest nodes (NtCN) to account inverse collisions and introduces errors of the order of $O(\Delta\xi)|f-f_M|$ in conservation of mass, momentum and energy. In order to eliminate these errors, we introduce a correction to the collision frequency using the method of least squares

$$\nu^*(\xi) = (1+a_0+a_1\xi_x+a_2\xi_y+a_3\xi_z+a_4(\xi_x^2+\xi_y^2+\xi_z^2))\nu(\xi), \tag{16}$$

where the coefficients a_i $(i=0,\ldots,4)$ are defined from the conservation laws (9), $\sum_i[-\nu^*(\xi_i)f(\xi_i)+\Phi(\xi_i)]\psi(\xi_i)\Delta\xi = 0$. Thus, this method of calculating the Boltzmann collision integral possesses all the properties (i–iii).

All three methods described above involve calculations of eight-dimensional integrals (11) or (13). For these calculations, the method of Korobov sequences [34] is applied. In the general case, Korobov's points inside an s-dimensional hypercube are defined as

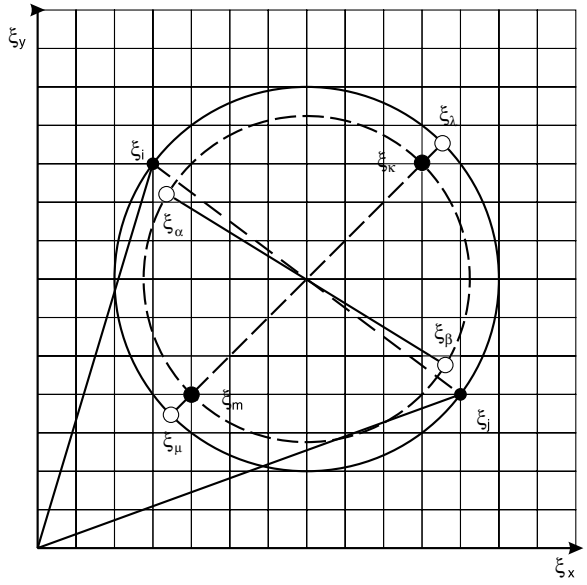

Fig. 4. Selection of nodes for NtCN method.

$$x_{r\kappa} = \{\kappa a_r^{p_\kappa}/p\}, \quad r = 1, 2, \ldots, s, \;\; \kappa = 1, 2, \ldots, p-1, \tag{17}$$

where p is a prime number, $a_r^{p_\kappa}$ are pre-calculated integer coefficients, and the brace denotes the reminder on dividing an integer by an integer. The velocity grid points closest to the selected Korobov's points are taken as the velocity grid points. The accuracy of this procedure is estimated as $O((\ln N_c)^{as}/N_c^a)$, where N_c is the number of quasi-random trials, and the exponent $a \geqslant 1$ depends on the smoothness of the integrated function (for a piecewise-constant function, $a = 1$). The above error is less than estimated error of $O(N_c^{1/2})$ for Monte Carlo methods of calculating multi-dimensional integrals.

The typical value of N_c in our simulations was equal to 34,000. We have accounted only for those collisions inside a sphere (with the center and radius defined by the characteristic parameters of the problem), for which inverse collisions also fall inside this sphere. Depending on the value of N_c, and the number of cells in velocity space, different Korobov's sequences were selected [34].

The calculations of the collision integral by the three methods described above satisfy the conservativity condition at the kinetic level [20]. Using any of them makes it possible to solve the BTE without splitting into collisionless flow and relaxation stages and use any other scheme of calculating a hyperbolic system with a source term. It is worth noting that the search for the best methods of calculating the Boltzmann collision integral continues. Many attempts have been explored [35], among them are the polar discretization of the velocity space [36], smoothing of the collision spheres [37] and smoothing the collision integral [38] in order to incorporate more points of the discrete velocity grid.

2.2. Shock structure calculations using the Boltzmann solver

In this Section, we illustrate application of the Boltzmann solver described above to simulation of the shock wave structure. The problem of shock wave structure is ideal for testing the quality of the numerical BTE solution, in particular, the accuracy of the nonlinear collision term. Shock wave describes collisional mixing of two equilibrium distributions with very different temperatures and mean velocities over a short distance of the order of several mean free paths. We have performed simulation of the shock wave structure for different Mach numbers and different models of intermolecular interactions and compared our results with the benchmark solutions, previous DSMC results and experimental data.

In our calculations, velocities are normalized to the thermal velocity $v_{\text{th}} = (2kT/m)^{1/2}$. The kinetic spatial scale is defined by the mean free path λ, which depends on the molecular interaction law, gas number density

n and temperature (for the HS model $\lambda = \left(\sqrt{2}\pi d^2 n\right)^{-1}$, where d is the diameter of molecules). The local Knudsen number is defined as $Kn = \lambda/L$, where L is a characteristic spatial dimension of the system. The Knudsen number for the free-stream conditions is denoted as $Kn_\infty = \lambda_\infty/L$, where λ_∞ is the mean free path for the free-stream with density n_∞ and temperature T_∞.

For a classical problem of the shock structure in a one-component monatomic gas, the VDFs upstream and downstream of the shock are defined as two Maxwellians with densities, temperatures and mean velocities given by the Rankine–Hugoniot relations. The computational domain in velocity space is selected as follows. The upper bound of the ξ_x velocity component, ξ_x^+, is equal to the maximum of two quantities, $u_1 + 3\sqrt{T_1}$ and $u_2 + 3\sqrt{T_2}$, where indexes 1 and 2 denote upstream and downstream values, correspondingly. The lower bound of the ξ_x velocity component, ξ_x^-, is defined as $u_2 - 3\sqrt{T_2}$. The ξ_y and ξ_z velocity bounds are from $-3\sqrt{T_2}$ to $3\sqrt{T_2}$. The velocity cell size is usually chosen as $\Delta\xi = \sqrt{T_1}/2$. We assume $n_1 = 1$, $T_1 = 1$, $u_1 = M\sqrt{5/6}$, where M is the Mach number.

The comparison with the benchmark results obtained by the conservation splitting method [39] and by the Ohwada's method [40] demonstrated agreement for gas density and temperature with an accuracy of 1% for the HS model. Fig. 5 compares calculated longitudinal and transversal temperatures inside a shock wave for different models of inter molecular interactions. The temperatures $T_\parallel$ and $T_\perp$ are defined as

$$T_\parallel = \frac{\int (\xi_x - u)^2 f \, d\boldsymbol{\xi}}{\int f \, d\boldsymbol{\xi}}; \quad T_\perp = \frac{\int ((\xi_y - v)^2 + (\xi_z - w)^2) f \, d\boldsymbol{\xi}}{\int f \, d\boldsymbol{\xi}} \tag{18}$$

and normalized to the downstream temperature T_2. Comparison of DNS and DSMC results [41] for Maxwell molecules demonstrates good agreement even for relatively coarse velocity grid in the Boltzman solver (24, 24, 12). The HS model yields shock thickness too small since the hard spheres are the most efficient scatterers.

Fig. 6 compares our computations with experiments for density and temperature profiles in the shock wave in rare gases for two different Mach numbers. The density profile in Argon for $M = 3.8$ is compared with an experiment by Alsmeyer [42]. The temperature profile in Helium for $M = 1.59$ is compared to the experiment [43]. The computations were performed for the Lennard-Jones interaction potential. The agreement of experimental and calculated profiles indicates the high accuracy of the Boltzmann solver.

Concluding this section, we should note that our goal here was not to study thoroughly the shock structure but only to validate the Boltzmann solver by comparison with benchmark solutions for simple models (such as the HS model), demonstrate that the method describes correctly non-equilibrium properties of the flow (such as longitudinal and transverse temperature, heat flux distributions, etc.), show that the method properly reacts on changing molecular interaction potential, and that it is capable of describing experimental data for the shock wave structure at different Mach numbers.

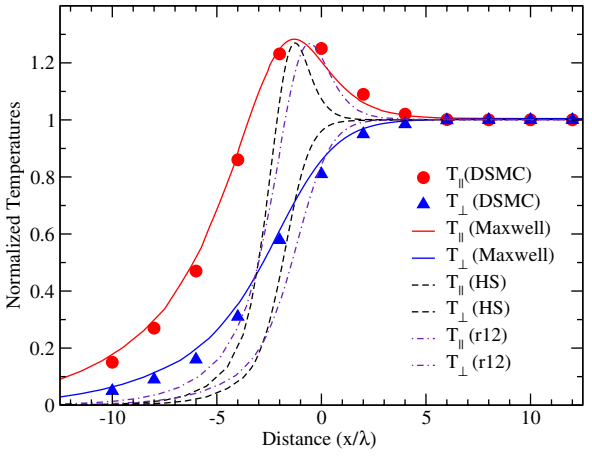

Fig. 5. Comparison of normalized longitudinal and transversal temperatures, $T_\parallel/T_2$ and $T_\perp/T_2$, for different models of intermolecular interactions for a shock wave at $M = 5$. Maxwell model (solid line), HS model (dashed line) and inverse power of 12 model (dash-dot line). Symbols denote DSMC results for Maxwell molecules.

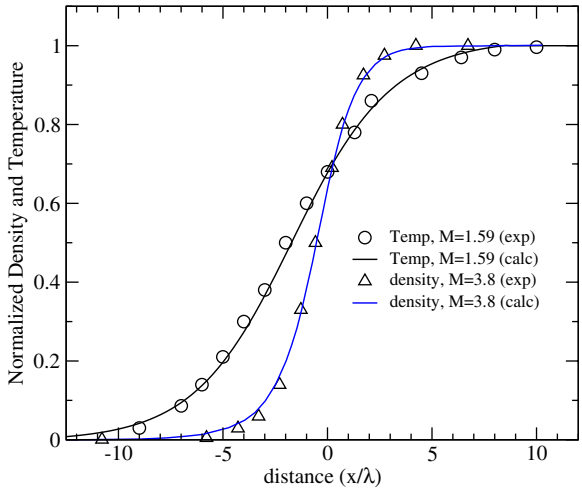

Fig. 6. Normalized gas density at $M = 3.8$ and temperature at $M = 1.59$ for a shock wave in argon (solid lines – calculations, symbols – experiment).

3. Kinetic schemes for continuum equations

Traditional numerical schemes of Computational Fluid Dynamics (CFD) are based on discretization of the fluid (Euler or NS) equations. Kinetic schemes differ from the traditional CFD schemes – they use the BTE for building numerical algorithms (see [44]). Kinetic schemes for the Euler equations were proposed in [45,46], and independently in [47,48]. The main idea of this approach was suggested earlier, in [49]. Kinetic schemes using *moments* of the equilibrium VDF were used by Deshpande with co-workers [50], and further developed and improved in [51,23,52,53]. We have used kinetic CFD scheme to facilitate coupling to the Boltzmann solver. Our implementation of the kinetic scheme for Euler and NS equations is described below.

3.1. Kinetic Euler solver

Our kinetic Euler scheme follows the equilibrium flux method by Pullin [45]. The main idea of this method is illustrated below. Consider Euler equations for monatomic gas in the form

$$\frac{\partial \mathbf{Y}}{\partial t} + \frac{\partial \mathbf{F}}{\partial x} + \frac{\partial \mathbf{G}}{\partial y} + \frac{\partial \mathbf{H}}{\partial z} = 0, \tag{19}$$

where

$$\begin{aligned} \mathbf{Y} &= \{\rho, \rho u, \rho v, \rho w, E\}, \\ \mathbf{F} &= \{\rho u, p/2 + \rho u^2, \rho v u, \rho u w, u(E+p)\}, \\ \mathbf{G} &= \{\rho v, \rho u v, p/2 + \rho v^2, \rho v w, v(E+p)\}, \\ \mathbf{H} &= \{\rho w, \rho u w, \rho v w, p/2 + \rho w^2, w(E+p)\}. \end{aligned} \tag{20}$$

Here $\rho = mn$ is the gas density, u,v and w are the mean gas velocities along the x, y and z axes, correspondingly, $E = 3/2\rho\ T + \rho(u^2 + v^2 + w^2)$ is energy, T is temperature and $p = nkT$ is gas pressure (in the considered case of monatomic perfect gas the ratio of the specific heats $\gamma = 5/3$).

The discretization of Eqs. (19) and (20) using the finite volume technique gives

$$\frac{\mathbf{Y}_{ijk}^{n+1} - \mathbf{Y}_{ijk}^{n}}{\Delta t} = -\left(\frac{\mathbf{F}_{i+1/2,j,k}^{n} - \mathbf{F}_{i-1/2,j,k}^{n}}{\Delta x} + \frac{\mathbf{G}_{i,j+1/2,k}^{n} - \mathbf{G}_{i,j-1/2,k}^{n}}{\Delta y} + \frac{\mathbf{H}_{i,j,k+1/2}^{n} - \mathbf{H}_{i,j,k-1/2}^{n}}{\Delta z} \right), \tag{21}$$

where $\mathbf{Y}^n_{ijk}$ is the cell averaged value of $\mathbf{Y}$ at a time t^n, $\mathbf{F}^n_{i+1/2,j,k}$, $\mathbf{G}^n_{i,j+1/2,k}$ and $\mathbf{H}^n_{i,j,k+1/2}$ are fluxes on cell faces along x, y and z, correspondingly. To obtain these fluxes, we calculate the integrals over the velocity distribution function, for instance

$$\mathbf{F}_{i+1/2,j,k} = \frac{1}{\Delta t}\int_{t^n}^{t^{n+1}}\int_{R^3}\psi\xi_x f(x_{i+1/2},t,\boldsymbol{\xi})\,\mathrm{d}\boldsymbol{\xi}\,\mathrm{d}t, \tag{22}$$

where ψ denotes the collision invariants (9). The fluxes $\mathbf{G}^n_{i,j+1/2,k}$ and $\mathbf{H}^n_{i,j,k+1/2}$ are calculated in a similar way. The required VDF at cell faces is taken in the form

$$f(x_{i+1/2},y_j,z_k,t,\boldsymbol{\xi}) = H[\xi_x]f^{\mathrm{l}}_{\mathrm{M}} + (1-H[\xi_x])f^{\mathrm{r}}_{\mathrm{M}}, \tag{23}$$

where $f^{\mathrm{l}}_{\mathrm{M}}$ and $f^{\mathrm{r}}_{\mathrm{M}}$ are Maxwellian distributions at the left and the right side of the face

$$f^{\mathrm{r}}_{\mathrm{M}} = \frac{\rho_{i+1/2}}{\left(\pi T^n_{i+1/2}\right)^{3/2}}\exp\left[-\frac{(\xi_x-u_{i+1/2,j,k})^2+(\xi_y-v_{i+1/2,j,k})^2+(\xi_z-w_{i+1/2,j,k})^2}{T^n_{i+1/2}}\right] \tag{24}$$

and $H[\xi]$ is the step function

$$H[\xi] = \left\{\begin{array}{ll} 1, & \xi>0 \\ 0, & \xi<0 \end{array}\right\}.$$

For the first order scheme, the values of macro-parameters at faces $\rho_{i+1/2,j,k}$, $u_{i+1/2,j,k}$, $v_{i+1/2,j,k}$, $w_{i+1/2,j,k}$, $T_{i+1/2,j,k}$ are calculated for the functions $f^{\mathrm{l}}_{\mathrm{M}}$ and $f^{\mathrm{r}}_{\mathrm{M}}$, using the known values of the macro-parameters in cells $x_{ij}(x_{i+1,j})$. For the second order scheme, the calculation of these macro-parameters is performed using standard methods of reconstruction using the values at $x_{i-1,j}x_{ij}, x_{i+1,j}(x_{i,j}x_{i+1,j}, x_{i+2,j})$ cells and corresponding limiters.

We illustrate the kinetic Euler scheme for a 2D transient simulation of an internal gas flow in a channel with a forward-facing step at $M=3$. The first and second order numerical schemes have been used with mesh refinement based on density gradient. The second-order scheme employs the minmod limiter or Van Leer limiter. Fig. 7 shows simulation results with a sensitivity parameter for mesh refinement equal to 0.025. The results are close to those of Ref. [54].

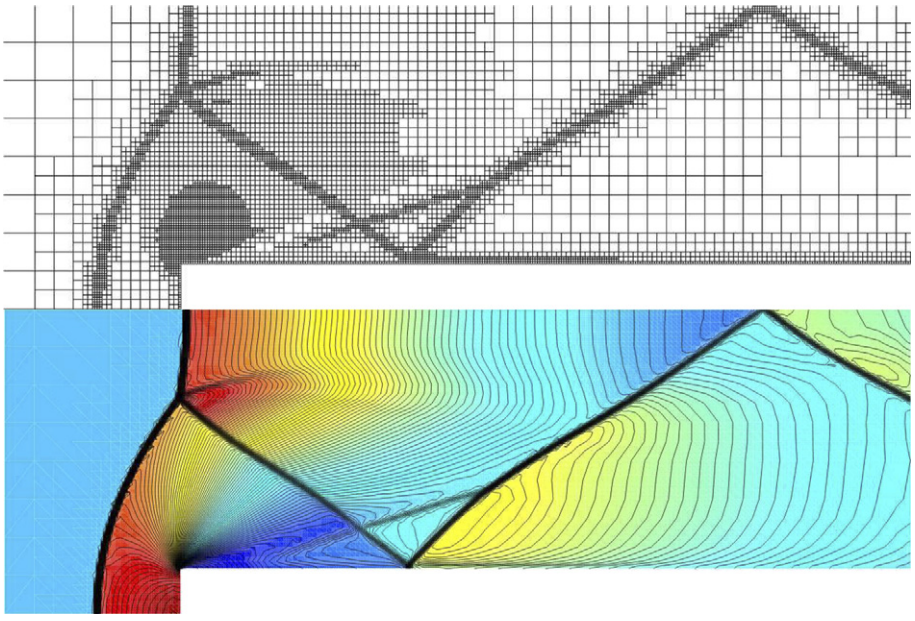

Fig. 7. Computational mesh (top) and gas density contours (bottom) at time $t=4$.

3.2. Kinetic NS solver

Minimizing the size of the kinetic domain where the Boltzmann equation is solved can increase the efficiency of computations. Using the NS solver instead of the Euler solver can expand the size of the continuum domain. The numerical scheme, which we use for the kinetic NS solver, was developed by Xu et al. and described in detail in several publications [23,55,56]. Here, we will only briefly outline the main features of this scheme.

The development of the kinetic NS solver is based on the solution of the BGK equation

$$\frac{\partial f}{\partial t} + \nabla_r \cdot (\boldsymbol{\xi} f) = \frac{f_{\mathrm{M}} - f}{\tau}, \tag{25}$$

where $\tau = \mu/p$ is the inter-collision time expressed though gas viscosity μ and pressure p, and f_{M} denotes a Maxwellian distribution. For the numerical solution of multi-dimensional problems we use directional splitting method to reduce the multi-dimensional equations to a set of one-dimensional equations. The gas kinetic BGK scheme is obtained by solving the BGK equation analytically. For a one-dimension case, the analytical solution has the form (the y and z dependencies are omitted)

$$f(x,\boldsymbol{\xi},t) = \frac{1}{\tau}\int_0^t f_{\mathrm{M}}(x^1,\boldsymbol{\xi},t^1)\mathrm{e}^{-(t-t^1)/\tau}\,\mathrm{d}t^1 + \mathrm{e}^{-t/\tau} f_0(x-\xi_x t,\boldsymbol{\xi},0), \tag{26}$$

where $x^1 = x - u(t-t^1)$ denotes the trajectory of the particles. Considering the solution at the discrete grid with the cells $(x_{i-1/2}, x_{i+1/2})$ the distribution function at an initial moment $f_0 = f(x,\boldsymbol{\xi},t=0)$ and a Maxwellian distribution $f_{\mathrm{M}}(x,\boldsymbol{\xi},t)$ around the cell faces can be constructed as

$$\begin{aligned} f_0 &= f_{\mathrm{M}}^{\mathrm{l}}[1 + a^{\mathrm{l}}x - \tau(a^{\mathrm{l}}\xi_x + A^{\mathrm{l}})](1 - H[x]) + f_{\mathrm{M}}^{\mathrm{r}}[1 + a^{\mathrm{r}}x - \tau(a^{\mathrm{r}}\xi_x + A^{\mathrm{r}})]H[x], \\ f_{\mathrm{M}}(x,t) &= f_{\mathrm{M0}}[1 + (1 - H[x])\bar{a}^{\mathrm{l}}x + H[x]\bar{a}^{\mathrm{r}}x + At]. \end{aligned} \tag{27}$$

where $f_{\mathrm{M0}} = f_{\mathrm{M}}(x,\boldsymbol{\xi},t=0)$ is defined below (see Eq. (31)). This approximation is consistent with the first order Chapman–Enskog expansion and allows one to account for a nonequilibrium VDF [56].

The values $a^{\mathrm{l,r}}$, $\bar{a}^{\mathrm{l,r}}$, $A^{\mathrm{l,r}}$ and A are polynomial functions in velocity space with coefficients depending on gradients of the conservative variables $\mathbf{Y}$

$$\begin{aligned} a^{\mathrm{l,r}} &= \alpha_1^{\mathrm{l,r}} + \alpha_2^{\mathrm{l,r}}\xi_x + \alpha_3^{\mathrm{l,r}}\xi_y + \alpha_4^{\mathrm{l,r}}\xi_z + \alpha_5^{\mathrm{l,r}}(\xi_x^2 + \xi_y^2 + \xi_z^2), \\ \bar{a}^{\mathrm{l,r}} &= \bar{\alpha}_1^{\mathrm{l,r}} + \bar{\alpha}_2^{\mathrm{l,r}}\xi_x + \bar{\alpha}_3^{\mathrm{l,r}}\xi_y + \bar{\alpha}_4^{\mathrm{l,r}}\xi_z + \bar{\alpha}_5^{\mathrm{l,r}}(\xi_x^2 + \xi_y^2 + \xi_z^2), \\ A^{\mathrm{l,r}} &= A_1^{\mathrm{l,r}} + A_2^{\mathrm{l,r}}\xi_x + A_3^{\mathrm{l,r}}\xi_y + A_4^{\mathrm{l,r}}\xi_z + A_5^{\mathrm{l,r}}(\xi_x^2 + \xi_y^2 + \xi_z^2), \\ A &= A_1 + A_2\xi_x + A_3\xi_y + A_4\xi_z + A_5(\xi_x^2 + \xi_y^2 + \xi_z^2). \end{aligned} \tag{28}$$

The parameters of the Maxwellian distribution $f_{\mathrm{M}}^{\mathrm{l,r}}$ are defined using the values of $\mathbf{Y}$ at $x_{i+1/2}$, and the coefficients $\alpha^{\mathrm{l,r}}$ are defined using the conservative variables, for example for a^{l}

$$\int_{R^3} a^{\mathrm{l}} f_{\mathrm{M}}^{\mathrm{l}} \psi\,\mathrm{d}\boldsymbol{\xi} = (\mathbf{Y}^{\mathrm{l}}(x_{i+1/2}) - \mathbf{Y}^{\mathrm{l}}(x_i))/(x_{i+1/2} - x_l). \tag{29}$$

The coefficients $A^{\mathrm{l,r}}$ are calculated to satisfy conservation laws

$$\int_{R^3} f_{\mathrm{M}}^{\mathrm{l,r}}(a^{\mathrm{l,r}}\xi_x + A^{\mathrm{l,r}})\psi\,\mathrm{d}\boldsymbol{\xi}. \tag{30}$$

The parameters $\mathbf{Y}_0$ of the Maxwellian distribution f_{M0} are calculated from the relation

$$\int_{R^3} f_{M0}\psi\,\mathrm{d}\boldsymbol{\xi} = \int_{\xi_x>0} f_{\mathrm{M}}^{\mathrm{l}}\psi\,\mathrm{d}\boldsymbol{\xi} + \int_{\xi_x<0} f_{\mathrm{M}}^{\mathrm{r}}\psi\,\mathrm{d}\boldsymbol{\xi} \tag{31}$$

and the coefficients $\bar{\alpha}^{\mathrm{l,r}}$ are calculated using the corresponding differences $(\mathbf{Y}_0 - \mathbf{Y}(x_i))/(x_{i+1/2} - x_i)$, $(\mathbf{Y}_0 - \mathbf{Y}(x_{i+1}))/(x_{i+1/2} - x_{i+1})$.

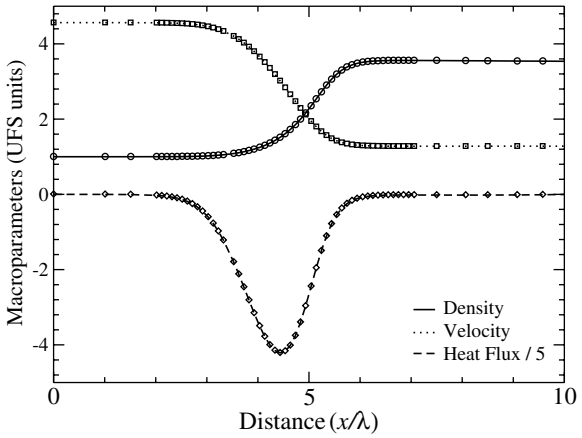

Fig. 8. Comparison of gas density, velocity and heat flux for a shock wave at $M = 5$ obtained from the kinetic NS solver with Pr correction (lines) and those from the classical NS solver (symbols).

For calculation of function A, the condition suggested in [55] is used

$$\frac{\partial}{\partial t}\int_{R^3}[f_{\mathrm{M}}(x_{i+1/2},t)-f(x_{i+1/2},t)]\psi\,\mathrm{d}\boldsymbol{\xi}|_{t=0}=0. \tag{32}$$

Having obtained the VDF on cell faces, the particle fluxes on faces are calculated by integration of the VDF with the collision invariants according to Eq. (22). This scheme incorporates the non-equilibrium character of the VDF by additional function $\tau f_{\mathrm{M}}(a^{\mathrm{l}}\boldsymbol{\xi}+A^{\mathrm{l}})$ and approximates the NS equations if $\tau(a^{\mathrm{l}}\boldsymbol{\xi}+A^{\mathrm{l}})\ll 1$.

The time step for Euler and NS solvers is calculated from the condition $\Delta t = \mathrm{CFL}*h/\max(|U+3\sqrt{T}|,|U-3\sqrt{T}|)$. The value of $\max(|U+3\sqrt{T}|,|U-3\sqrt{T}|)$ corresponds to the value of $|\xi_{\max}|$ for the Boltzmann solver. When the local time step is used, the values of U and T are selected locally based on the flow properties at the previous time step. The CFL number is set to 0.5 in most cases. When coupling continuum and kinetic solutions, the time steps in mixed cells at the interface between the kinetic and continuum domains must be as close as possible; this can be achieved by varying the local CFL number.

3.2.1. Prandtl number correction

It is well known that the BGK model results in an incorrect Prandtl number, $Pr = 1$. To introduce Pr number correction, we calculate the heat flux Q on cell faces using polynomial interpolation of the VDF and then modify the value of the energy flux at faces by adding the $(Pr^{-1}-1)Q$ correction. This algorithm of Pr correction was tested for the shock wave structure for different Mach numbers ($M = 1.5, 3, 5, 10$) and for different temperature dependence of the viscosity coefficient. The results of the calculations were compared with the benchmark calculations for the classical NS solver [23]. Fig. 8 shows results for $M = 5$ and $Pr = 2/3$. The results of classical NS solver and kinetic NS solver coincide with each other with high accuracy for all Mach numbers. Similar results were reported in [56] for $M = 10$ and different Pr numbers.

4. Domain decomposition and coupling algorithm

The main problem of unified methods is how to separate kinetic and continuum regions. Different continuum breakdown criteria are discussed in [10,57]. In our hybrid solver the adequate switching criterion is important because the wrong domain decomposition could lead to a non-positive distribution function when the NS solution is coupled with the Boltzmann solution. In the present paper, we used the following switching criteria:

$$S_\rho = Kn\frac{1}{\rho}|\nabla\rho|, \tag{33}$$

$$S_{\mathrm{NS}} = Kn\sqrt{\left(\frac{\nabla p}{p}\right)^2+\frac{1}{U^2}\left[\left(\frac{\partial u}{\partial x}\right)^2+\left(\frac{\partial v}{\partial y}\right)^2+\left(\frac{\partial w}{\partial z}\right)^2\right]}, \tag{34}$$

where all values are given in dimensionless form, and *Kn* denotes the *local* Knudsen number. For gas flow around a cylinder of radius R, $Kn = \lambda/R$, where λ is the local mean free path. The first breakdown parameter, S_ρ, based on the density gradient was used by Roveda et al. [58] among others.

If S is greater than some threshold value, then the kinetic solver is used. The applicability of different criteria and the ways to choose the threshold value depend on the type of problem being studied. We have found that for supersonic external flows the criterion (34) correctly gives the non-equilibrium domain near the shock wave and behind solid bodies at moderate Knudsen numbers. At small Knudsen numbers ($Kn \ll 1$) non-equilibrium domain behind the bodies appears to be too small. The criterion (34) gives extended kinetic regions in the low-speed regions behind the bodies and enables successful coupling of the NS and Boltzmann solvers. It should be noted that the breakdown criteria derived from continuum solutions might not be appropriate for all cases, and more computationally expensive breakdown criteria derived from the kinetic solvers might be necessary for some problems [2,57,9].

4.1. Coupling kinetic and continuum solvers

Coupling of Boltzmann and Euler solvers consists of the following. The boundary conditions for the Euler equations are determined from the moments of the VDF in the two neighboring cells. From the known VDF, parameters of the corresponding Maxwellian distribution are defined. The boundary conditions for the Boltzmann equation are obtained assuming Maxwellian VDF in the continuum cells.

The coupling of the Boltzmann and NS solvers consists of the following. On each time step, a continuum cell is considered, which is a neighbor to a kinetic (Boltzmann) cell. In this continuum cell, a velocity grid is introduced which is identical to that in the kinetic cell. On this velocity grid, the following distributions functions are constructed $f_0 = f_M^1[1 - \tau(a^1\xi_n + A^1)]$ on each face where ξ_n is the normal velocity to the cell face. The parameters of the Maxwellian distribution function g^1 are calculated using the macroparameters in the continuum cell and the coefficients of the polynomial a^1 are calculated using the gradients of the macroparameters in the continuum and the neighboring kinetic cells. The coefficients of the polynomial A^1 are then calculated using the relationship of conservation $\int f_M^1(a^1\xi_n + A^1)\psi_\alpha \, d\xi = 0$ of the moments on the discreet velocity grid.

The key to the hybrid computations is consistency in connecting kinetic and gas-dynamic solutions. The NS equations solved by CFD should be consistent with the kinetic equation solved in nonequilibrium regions. The gas kinetic CFD scheme is based on the BGK kinetic equation, taking into account different models of molecular collisions by relating the collision frequency to viscosity and *Pr* number correction. However, when the CFD solution is employed as the boundary condition for the kinetic solution, the distribution function consistent with the Boltzmann kinetic equation must be used. It is theoretically consistent to specify this distribution function in the Chapman–Enskog form

$$f(\mathbf{C}) = f_M(\mathbf{C})\left(1 + q_i C_i\left(\frac{2}{5}C^2 - 1\right) + \tau_{ij}C_iC_j\right) = f_M(\mathbf{C})\Gamma(\mathbf{C}), \tag{35}$$

where $\mathbf{C} = (\boldsymbol{\xi} - \mathbf{U})/v_{th}$, $q_i = -\dfrac{\chi}{p v_{th}}\left(\dfrac{2m}{kT}\right)^{1/2}\dfrac{\partial T}{\partial x_i}$ is the dimensionless heat flux vector and $\tau_{ij} = -\dfrac{\mu}{p}\left(\dfrac{\partial u_i}{\partial x_j} + \dfrac{\partial u_j}{\partial x_i} - \dfrac{2}{3}\delta_{ij}\dfrac{\partial u_k}{\partial x_k}\right)$ is the dimensionless shear stress tensor. The transport coefficients (viscosity μ and thermal conductivity χ) depend on specific models of molecular interactions. The Chapman–Enskog parameter Γ is a good predictor of non-equilibrium conditions [57]. When Γ is sufficiently far from unity, the NS equations are expected to fail and the kinetic solver must be used.

In our work we used the VDF (27) as a boundary condition for the Boltzmann solver. To verify the validity of such an approach, test simulations for both VDF (27) and (35) were performed for a shock wave. Fig. 9 shows spatial distributions of macroparameters for $M = 5$ obtained by the two methods and demonstrates the validity of using the VDF (27) in this particular case. The reason for the close agreement of the two methods lies in the fact that coupling takes place in the area where the distribution function is close to equilibrium (locally, $Kn \ll 1$), and the difference between the VDFs (27) and (35) is small. We have observed that the expansion of the continuum domain could result in negative values of the distribution function and incorrect computation of the flow field. Generally, the choice of distribution function at the interface should be consistent with the continuum breakdown criteria, and vice versa.

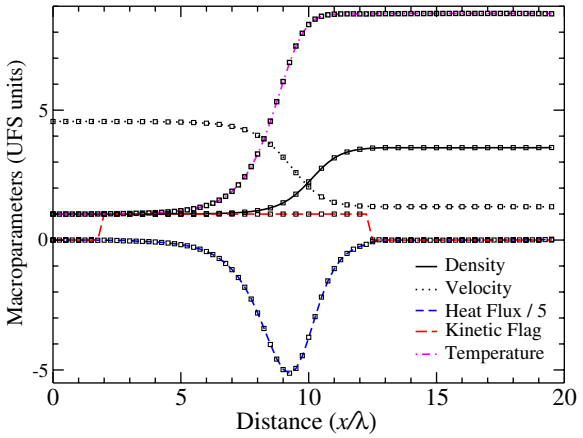

Fig. 9. UFS calculations of SW structure at $M = 5$. Kinetic flag indicates kinetic (=1) and continuum (=0) domains. Lines are results of simple VDF (27) at the interface, symbols are for the VDF (35) at the interface.

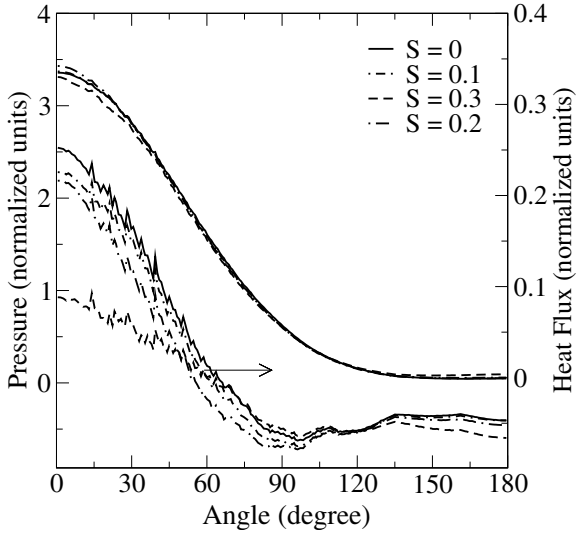

Fig. 10. Pressure and heat flux over cylinder surface as a function of angle for different values of the breakdown parameter S.

4.2. Effect of breakdown parameter

We have studied the influence of the breakdown parameter on the flow characteristics calculated by the UFS. Fig. 10 shows the gas pressure and the heat flux distributions over the cylinder surface calculated with different breakdown parameters, S, for supersonic gas flow around a cylinder at $M = 2$, $Kn_\infty = 0.1$ and $T_w = 2.28$. One can see that all curves converge at small S numbers when the Boltzmann region grows. At the same time, by decreasing the S value, the computation time increases. Therefore, for quick results one can use large values of S, if precision of the order of 10% is satisfactory.

5. UFS demonstration

In this section we demonstrate the UFS capabilities for simulation of external and internal flows for different Knudsen and Mach numbers.

5.1. External flows

The flow of single-component monatomic gas around a cylinder at $M = 3$ was studied in a wide range of Kn_∞ numbers (0.001–10) with different criteria of domain decomposition. The boundary condition on the surface of the cylinder corresponds to the diffuse reflection with the temperature of the wall $T_w = 4$. Fig. 11 shows the results of computations with the Boltzmann and Euler solvers. The continuum breakdown criterion (34) is used with the value of the breakdown parameter equal to 0.3. The mesh refinement criterion is $\beta = \log(\rho) + \log(u)$.

The distributions of pressure, shear stress and the heat flux over the surface of cylinder for $M = 2$, $Kn_\infty = 0.1$ and $T_w = 2.28$ are shown in Fig. 12 for different levels of mesh refinement near the surface. The

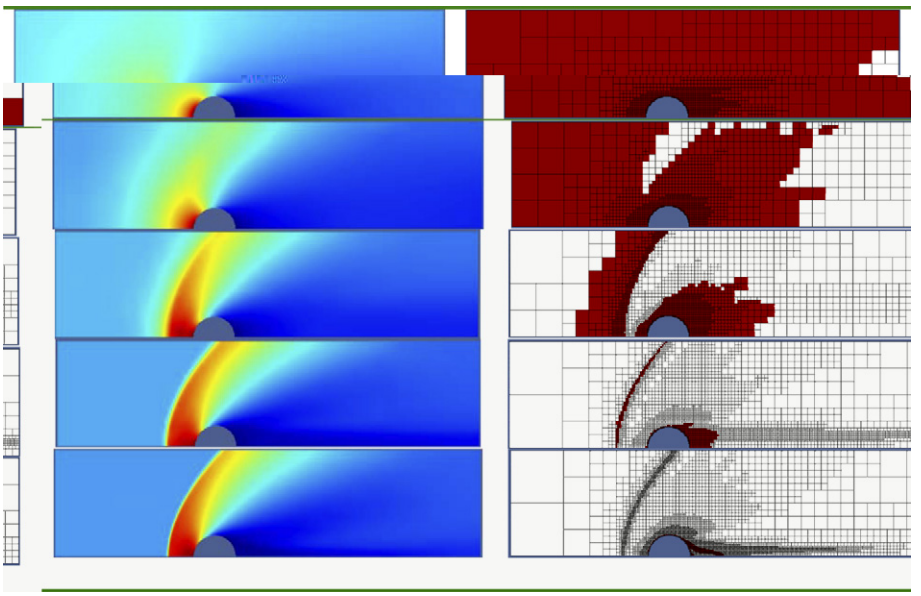

Fig. 11. Gas flow around a cylinder for $M = 3$, for different Kn numbers ($Kn_\infty = \lambda_\infty/R = 5, 1.5, 0.5, 0.05, 0.005$). On the left side are the density profiles, on the right side are the computational grid with kinetic (dark) and continuum (white) domains.

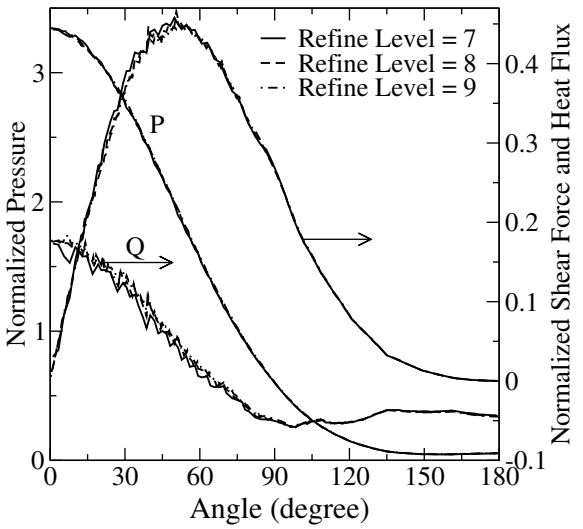

Fig. 12. Pressure, shear stress and heat flux distribution over the cylinder surface.

refinement level of 7 corresponds to the cell size of the order of λ. One can see that the shear force is a relatively smooth function of angle around the cylinder. Although not directly compared here, the shear force appears to be smoother than what is expected from a conventional NS formulation [59,60]. The heat flux is also a relatively smooth function; it becomes smoother as the refinement level increases. As noted in [59–61], the non-smoothness and non-orthogonality at mesh refinement and cut-cell boundaries of hierarchically-based, adaptively refined grids can introduce non-positive discrete representations when applied to solving the NS equations. This is due to representation of the viscous fluxes by higher order derivatives of the cell-centered data in a non-positive fashion, which for low cell Reynolds and Peclet numbers, can cause at best, non-smooth solutions and at worst, instabilities that may not be damped by the temporal scheme [59]. The approach presented here might overcome this deficiency, although more investigations are in order.

We have verified that increasing the mesh resolution around solid bodies does not lead to an increase in the noise. This result is also encouraging since, typically, NS results become noisier when increasing the spatial grid resolution near the surface.

Fig. 13 compares the calculated drag coefficient with experimental data [62] for $M = 1.96$ and $M = 4$. It is seen that the UFS simulations agree well with the experimental data.

5.2. Simulations of internal flows

The UFS has been tested for simulations of internal flows in channels and nozzles. Fig. 15 shows examples of 2D simulations of a short channel and a nozzle for two different *Kn* numbers. For the channel simulations, the geometry and flow conditions correspond to Ref. [63]. The BTE-NS option of the UFS solver with second order spatial discretization scheme was used in these simulations. The boundary conditions on the left boundary are $\rho_{in} = p_{in} = 1.5$, the boundary condition on the right boundary is $p_{out} = 0.5$. For the nozzle simulations, the geometry and flow conditions correspond to Ref. [64]. The BTE-Euler option of the UFS with the first order numerical scheme was used, the grid adaptation is based on $\beta = \log(\rho) + \log(u)$. One can see in Fig. 14 that significant continuum regions exist at low Knudsen numbers which can be simulated by the NS solver.

5.3. 3D simulations

The parallel version of the UFS has been developed with the possibility of dynamic domain decomposition and dynamic load balancing between different processors. The procedure of domain decomposition was performed using space-filling curves (SFC). During sequential traversing of the cells by natural order, the physical space is filled with curves in *N*-order (Morton ordering). After this ordering of cells, all cells can be considered

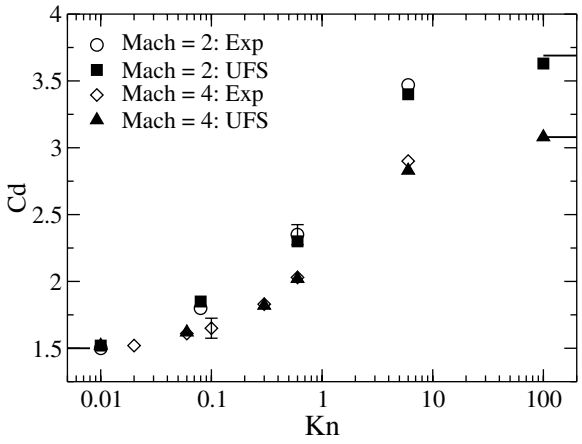

Fig. 13. Drag coefficient versus *Kn* number. Comparison of UFS simulations with experiment. Solid lines indicate the free molecular flow and continuum limits.

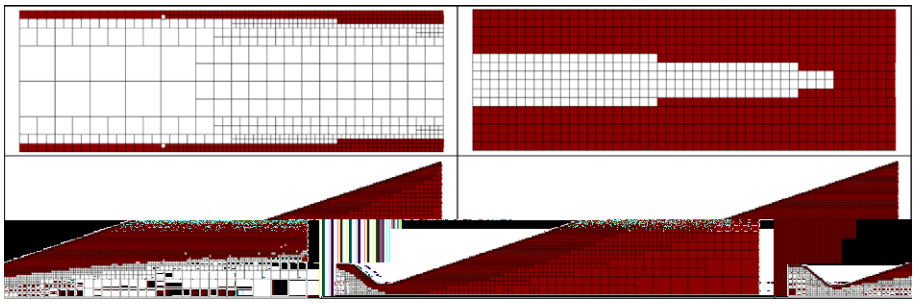

Fig. 14. Kinetic (dark) and continuum (white) domains for a 2D micro channel (top) for $Kn = 0.01$ (left) and $Kn = 0.1$ (right) and a nozzle (bottom) for $Kn = 0.05$ (left) and $Kn = 0.005$ (right).

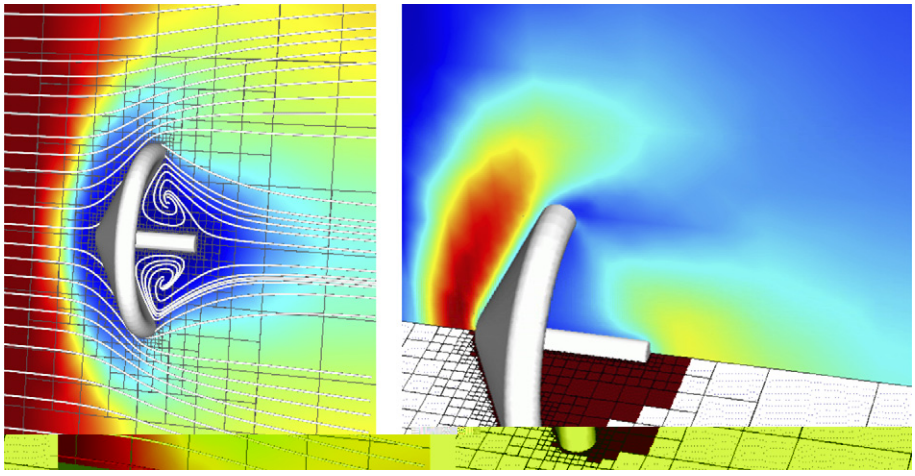

Fig. 15. Streamlines, Mach number and computational mesh (on the left). Gas temperature in the vertical plane, kinetic (brown) and continuum (white) domains in the horizontal plane (on the right). (For interpretation of the references in colour in this figure legend, the reader is referred to the web version of this article.)

as a one-dimensional array. A weight is assigned to each cell, which is proportional to the CPU time required to perform computations in this cell. Furthermore, the array modified with corresponding weights is subdivided into sub-arrays equal to the number of processors, in such a way that the weights of the sub-arrays are approximately the same. It was demonstrated that this method allows rather efficient domain decomposition between different processors.

An example of 3D simulations on a 7-processor Linux cluster is shown in Fig. 15 for the Inflatable Reentry Vehicle Experiment (IRVE). The flow conditions correspond to 91 km altitude ($Kn_\infty = 0.01$ and $M = 3.94$), at zero angle of attack [65]. Fig. 15 shows streamlines, Mach number and computational mesh (on the left), the gas temperature T (normalized on T_∞) in the vertical plane, as well as kinetic (red) and continuum (blue) domains in the horizontal plane (on the right). The flow recirculation is observed in the kinetic domain behind the body. The streamlines are not closed due to 3D effects.

6. Summary and outlook

We have developed a Unified Flow Solver with adaptive mesh and algorithm refinement based on the direct numerical solution of the Boltzmann equation coupled to a kinetic CFD model. Our strategy allows easy coupling of the Boltzmann and CFD solvers in a hybrid code with automatic domain decomposition. We have demonstrated the UFS capabilities for several one-component gas flows and have confirmed that the hybrid method results in significant savings by limiting expensive kinetic solutions only to the regions where they are

needed. We have demonstrated that the UFS can automatically introduce or remove kinetic patches to maximize accuracy and efficiency of simulations. Future work will focus on UFS extensions to reactive gas mixtures, aiming to produce an efficient tool for solving practical problems of molecular gas flows with various degree of rarefaction.

Acknowledgments

Thanks are due to Dr. S. Bayyuk for his contributions at the early stages of the UFS development. This work is supported by the US Air Force SBIR Project F33615-03-M-3326. The authors would like to thank the project monitor, Mr. Eswar Josyula for enthusiastic support and useful discussions. The work of the Moscow group is also supported in part by the Russian Foundation for Basic Research, Grant No. 04-01-00347. The authors would like to thank the anonymous referees for their insight and useful comments, which helped to improve the paper.

References

[1] H.S. Wijesinghe, N.G. Hadjiconstantinou, A discussion of hybrid atomistic-continuum methods for multiscale hydrodynamics, Int. J. Multiscale Comput. Eng. 2 (2004) 189.
[2] V.I. Kolobov, S.A. Bayyuk, R.R. Arslanbekov, V.V. Aristov, A.A. Frolova, S.A. Zabelok, Construction of a unified continuum/kinetic solver for aerodynamic problems, AIAA J. Spacecraft Rockets 42 (2005) 598–605.
[3] J. Eggers, A.E. Beylich, Development of a hybrid scheme and its application to a flat plate flow, in: J. Harvey, G. Lord (Eds.), Proceedings of the 19th International Symposium on Rarefied Gas Dynamics, vol. 2, Oxford University Press, Oxford, 1995, pp. 1216–1222.
[4] J.F. Bourgat, P. Le Tallec, M.D. Tidriri, Coupling Boltzmann and Navier–Stokes equations by friction, J. Comput. Phys. 127 (1996) 227.
[5] D.C. Wadsworth, D.A. Erwin, Two-dimensional hybrid continuum/particle approach for rarefied flows, AIAA paper 92-2975, 1992.
[6] S. Tiwari, A. Klar, An adaptive domain decomposition procedure for Boltzmann and Euler equations, J. Comput. Appl. Math. 90 (1998) 223.
[7] P. Le Tallec, F. Mallinger, Coupling Boltzmann and Navier–Stokes equations by half fluxes, J. Comput. Phys. 136 (1997) 51.
[8] S. Tiwari, Coupling of the Boltzmann and Euler equations with automatic domain decomposition, J. Comput. Phys. 144 (1998) 710.
[9] T.Ohsawa, T.Ohwada, Deterministic hybrid computation of rarefied gas flows, RGD23, in: Andrew D. Ketsdever, E.P. Munz (Eds.), Rarefied Gas Dynamics: 23rd International Symposium, AIP Conference Proceedings, vol. 663, 2003, pp. 931–938.
[10] H.A. Carlson, R.Roveda, I.D. Boyd, G.V. Candler, A hybrid CFD-DSMC method of modeling continuum-rarefied flows, AIAA paper 2004-1180.
[11] H.S. Wijesinghe, R. Hornung, A.L. Garsia, H.N. Hadjiconstantinou, Three-dimensional hybrid continuum-atomistic simulations for multiscale hydrodynamics, J. Fluids Eng. 126 (2004) 768–777.
[12] K. Morinishi, Numerical simulation for gas microflows using Boltzmann equation, Comput. Fluids 70 (2005) 303.
[13] N. Crouseilles, P. Degond, M. Lemou, A hybrid kinetic/fluid models for solving the gas dynamics Boltzmann–BGK equation, J. Comput. Phys. 199 (2004) 776.
[14] A.E. Beylich, Solving the kinetic equation for all Knudsen numbers, Phys. Fluids 12 (2000) 444.
[15] A.E. Beylich, Kinetics of thermalization in shock waves, Phys. Fluids 14 (2002) 2683.
[16] A.L. Garsia, J. B Bell, W.Y. Crutchfield, B.J. Alder, Adaptive mesh and algorithm refinement using direct simulation Monte Carlo, J. Comput. Phys. 54 (1999) 134.
[17] D.B. Hash, H.A. Hassan, Two-dimensional coupling issues of hybrid DSMC/Navier–Stokes solvers, AIAA paper 97-2507, 1997.
[18] H.A. Carlson, R.Roveda, I.D. Boyd, G.V. Candler, A hybrid CFD-DSMC method of modeling continuum-rarefied flows, AIAA paper 2004-1180, 2004.
[19] V.V. Aristov, A.A. Frolova, S.A. Zabelok, V.I. Kolobov, S.A. Bayyuk, R.R. Arslanbekov, Coupling direct Boltzmann and continuum flow solvers, in: M.Capitelli (Ed.), Rarefied Gas Dynamics, AIP Conference Proceedings, vol. 762, NY, 2005, pp. 96–101.
[20] V.V. Aristov, Direct Methods for Solving the Boltzmann Equation and Study of Non-Equilibrium Flows, Kluwer Academic Publishers, Dordrecht, 2001.
[21] F.G. Tcheremissine, Direct numerical solution of the Boltzmann equation, in: M. Capitelli (Ed.), Rarefied Gas Dynamics, AIP Conference Proceedings, NY, vol. 762, 2005, pp. 677–685.
[22] S.P. Popov, F.G. Tcheremissine, Method of joint solution of the Boltzmann and Navier–Stokes equations, in: M. Capitelli (Ed.), Rarefied Gas Dynamics, AIP Conference Proceedings, NY, vol. 762, 2005, pp. 82–87.
[23] K. Xu, A gas-kinetic BGK scheme for the Navier–Stokes equations and its connection with artificial dissipation and Godunov method, J. Comput. Phys. 171 (2001) 289–335.
[24] T. Ohwada, S. Fukata, Simple derivation of high-resolution schemes for compressible flows by kinetic approach, J. Comput. Phys. 211 (2006) 424.

[25] S. Popinet, Gerris: a tree-based adaptive solver for the incompressible Euler equations in complex geometries, J. Comput. Phys. 190 (2003) 572.
[26] C. Cercignani, The Boltzmann Equation and its Applications, Springer-Verlag, 1988.
[27] S.P. Popov, F.G. Cheremisin, A conservative method for solving the Boltzmann equation with centrally symmetric interaction potentials, Comput. Math. Math. Phys. 39 (1999) 156.
[28] N. Bellomo, R. Gatignol (Eds.), Lecture Notes on the discretization of the Boltzmann Equation, World Scientific, 2003.
[29] D.B. Goldstein, B. Sturtevant, J.E. Broadwell, Investigation of the motion of the discrete velocity gases, in: E.P. Muntz et al. (Eds.), Proceedings of the16th International Symposium on RGD, in Series: Progress in Astronautics and Aeronautics 118, 1989, p. 100.
[30] C. Buet, A discrete velocity scheme for the Boltzmann operator of rarefied gas dynamics, Trans. Theo. Stat. Phys. 25 (1996) 33.
[31] F. Rogier, J.A. Schneider, A direct method for solving Boltzmann equation, Trans. Theo. Stat. Phys. 23 (1–3) (1994) 313–338.
[32] Z. Tan, P.L. Varghese, The Δ–ε method for the Boltzmann equation, J. Comput. Phys. 110 (1994) 327.
[33] F.G. Tcheremissine, Solution to the Boltzmann kinetic equation for high-speed flows, Comput. Math. Math. Phys. 46 (2006) 315.
[34] N.M. Korobov, Exponential Sums and Their Applications, Springer, 2001, 232p;
N.M. Korobov, Theoretico-Numerical Methods in Approximate Analysis, Moscow, 2004 (in Russian).
[35] P. Degond, L. Pareschi, G. Russo (Eds.), Modeling and Computational methods for Kinetic Equations, Birkhauser, Boston, 2004, p. 356.
[36] L. Preziozi, L. Rondoli, Conservative discretization of the Boltzmann equation and the semicontinuous model, in: Lecture Notes on the Discretization of the Boltzmann Equation, Chapman Hall/CRC Press, 2002.
[37] C. Buet, S. Gordier, P. Degond, Regularized Boltzmann operators, Comput. Math. Appl. 35 (1998) 55.
[38] D. Gorsch, Generalized discrete velocity models, Math. Models Meth. Appl. Sci. 12 (2002) 49.
[39] V.V. Aristov, F.G. Tcheremissine, Shock wave structure in monatomic gas at power potentials, Fluid Dyn. (2) (1982) 179–183.
[40] T. Ohwada, Structure of normal shock waves on the basis of the Boltzmann equation for hard-spheres molecules, Phys. Fluids A5 (1993) 217–234.
[41] E. Josyula, K. Xu, D.C. Wadsworth, Testing continuum and non-continuum descriptions in high speed flows, AIP Conf. Proc. 762 (2004) 1217.
[42] H. Alsmeyer, Density profiles in argon and nitrogen shock waves measured by the absorption of an electron beam, J. Fluid. Mech. 74 (1976) 497.
[43] E.P. Muntz, L.N. Harnett, Molecular velocity distribution function measurement in a normal shock wave, Phys. Fluids 12 (1969) 2027–2035.
[44] Y. Sone, Kinetic Theory and Fluid Dynamics, Burkhausen, Boston, 2002.
[45] D.I. Pullin, Direct simulation methods for compressible inviscid ideal gas flow, J. Comput. Phys. 34 (1980) 231.
[46] R.D. Reitz, One dimensional compressible gas dynamics calculations using the Boltzmann equations, J. Comput. Phys. 42 (1981) 108.
[47] V.V. Aristov, F.G. Tcheremissine, Solving the Euler and Navier–Stokes equations on the basis of the operator splitting of the kinetic equations, Doklady USSR Acad. Sci. 272 (1983) 555.
[48] V.V. Aristov, F.G. Tcheremissine, The kinetic numerical method for rarefied and continuum gas flows, in: O.M. Belotserkovskii et al. (Eds.), Rarefied Gas Dynamics, vol. 1, Plenum Press, NY, 1985, p. 269.
[49] V.V. Potkin, A kinetic scheme for gas-dynamic equations in Lagrange coordinates, J. Comp. Math. Math. Phys. 15 (1975) 227.
[50] J.C. Mandal, S.M. Deshpande, Kinetic flux vector splitting for Euler equations, Comput. Fluids 23 (1994) 447.
[51] S.Y. Chou, D. Baganoff, Kinetic flux-vector splitting for the Navier–Stokes equations, J. Comput. Phys. 130 (1997) 217.
[52] T. Ohwada, On the construction of kinetic schemes, J. Comput. Phys. 177 (2002) 156.
[53] T. Ohwada, S. Kobayashi, Management of discontinuous reconstruction in kinetic schemes, J. Comput. Phys. 197 (2004) 116.
[54] C. Kim, A. Jameson, A robust and accurate LED-BGK solver on unstructured adaptive meshes, J. Comput. Phys. 143 (1998) 598.
[55] Q. Li, S. Fu, K. Xu, A compressible Navier–Stokes flow solver with scalar transport, J. Comput. Phys. 204 (2005) 692.
[56] G. May, B. Srinivasan, A. Jameson, An improved gas-kinetic BGK finite-volume method for three-dimensional transonic flow, J. Comput. Phys., 2006, doi:10.1016/j.jcp.2006.05.027.
[57] I.D. Boyd, Predicting breakdown of the continuum equations under rarefied flow conditions, in: Andrew D. Ketsdever, E.P. Munz (Eds.), Rarefied Gas Dynamics: 23rd International Symposium, AIP Conference Proceedings 663, 2003, pp. 899–906.
[58] R. Roveda, D.B. Goldstein, P.L. Varghese, Hybrid Euler/direct simulation Monte Carlo calculation of unsteady slit flow, J. Spacecraft Rockets 37 (2000) 753.
[59] W.J. Coirier, An adaptively refined Euler and Navier–Stokes solution on an unstructured quadtree-based grid, Ph.D. thesis, Aerospace Engineering Department, The University of Michigan, 1994.
[60] W.J. Coirier, A. Cartesian, Cell-based approach for adaptively-refined solutions of the Euler and Navier–Stokes equations, NASA TM 106786 and AIAA-95-0566.
[61] F.E. Ham, F.S. Lien, A.B. Strong, A cartesian grid method with transient anisotropic adaptation, J. Comput. Phys. 179 (2002) 469.
[62] G.J. Maslach, S.A. Schaaf, Cylinder drag in the transition from continuum to free-molecule flow, Phys. Fluids 6 (3) (1963) 315–321.
[63] K. Xu, Z. Li, Microchannel flow in the slip regime: gas-kinetic BGK—Burnett solutions, J. Fluid Mech. 513 (2004) 87.
[64] R.L. Bayt, Analysis, fabrication and testing of a MEMS-based micropropulsion system, PhD thesis, MIT 1999.
[65] J.N. Moss, C.E. Glass, B.R. Hollis, J.W. van Norman, Low-density aerodynamics of the inflatable reentry vehicle experiment (IRVE), AIAA paper 2006-1189.